

https://dspace.org/

Nuclear level density and ray strength function of 67Ni and the impact on the i process

V.W. Ingeberg; S. Siem; Mathis Wiedeking; A. Choplin; S. Goriely ...

AMER PHYSICAL SOC
https://hdl.handle.net/10539/46285
WOS

Downloaded from a DSpace repository. https://dspace.org/

Nuclear level density and γ-ray strength function of ^{67}Ni and the impact on the *i* process

V. W. Ingeberg,[1,2,*] S. Siem,[1,2,†] M. Wiedeking,[3,4,5] A. Choplin,[6] S. Goriely,[6] L. Siess,[6] K. J. Abrahams,[7] K. Arnswald,[8] F. Bello Garrote,[1] D. L. Bleuel,[9] J. Cederkäll,[10,11] T. L. Christoffersen,[1] D. M. Cox,[12,13] H. De Witte,[14] L. P. Gaffney,[11,‡] A. Görgen,[1,2] C. Henrich,[15] A. Illana,[14,§] P. Jones,[4] B. V. Kheswa,[1,‖] T. Kröll,[15] S. N. T. Majola,[4,‖] K. L. Malatji,[4,16] J. Ojala,[12,13] J. Pakarinen,[12,13] G. Rainovski,[17] P. Reiter,[8] M. von Schmid,[15] M. Seidlitz,[8] G. M. Tveten,[1] N. Warr,[8] and F. Zeiser[1]
(The ISOLDE Collaboration)

[1]*Department of Physics, University of Oslo, NO-0316 Oslo, Norway*
[2]*Norwegian Nuclear Research Centre, NO-0316 Oslo, Norway*
[3]*Nuclear Science Division, Lawrence Berkeley National Laboratory, Berkeley, California 94720, USA*
[4]*SSC Laboratory, iThemba LABS, P. O. Box 722, 7129 Somerset West, South Africa*
[5]*School of Physics, University of the Witwatersrand, 2050 Johannesburg, South Africa*
[6]*Institut d'Astronomie et d'Astrophysique, Université Libre de Bruxelles (ULB), Campus de la Plaine, CP 226, 1050 Brussels, Belgium*
[7]*Department of Physics, University of the Western Cape, P/B X17 Bellville 7535, South Africa*
[8]*Institut für Kernphysik, University of Cologne, D-50937 Cologne, Germany*
[9]*Lawrence Livermore National Laboratory, 7000 East Avenue, Livermore, California 94550-9234, USA*
[10]*Physics Department, University of Lund, Box-118, SE-22100 Lund, Sweden*
[11]*ISOLDE, EP Department, CERN, CH-1211 Geneva, Switzerland*
[12]*Department of Physics, University of Jyväskylä, P. O. Box 35, FIN-40014 Jyväskylä, Finland*
[13]*Helsinki Institute of Physics, University of Helsinki, P. O. Box 64, FIN-00014 Helsinki, Finland*
[14]*Instituut voor Kern- en Stralingsfysica, K.U. Leuven, Celestijnenlaan 200D, B-3001 Leuven, Belgium*
[15]*Institut für Kernphysik, Technische Universität Darmstadt, D-64289 Darmstadt, Germany*
[16]*Department of Physics, Stellenbosch University, Private Bag X1, Matieland 7602, South Africa*
[17]*Faculty of Physics, St. Kliment Ohridski University of Sofia, BG-1164 Sofia, Bulgaria*

(Received 14 July 2023; revised 14 November 2024; accepted 24 December 2024; published 16 January 2025)

Proton-γ coincidences from (d, p) reactions between a ^{66}Ni beam and a deuterated polyethylene target have been analyzed with the inverse-Oslo method to find the nuclear level density (NLD) and γ-ray strength function (γSF) of ^{67}Ni. The ^{66}Ni(n, γ) capture cross section has been calculated using the Hauser-Feshbach model in TALYS using the measured NLD and γSF as constraints. The results confirm that the ^{66}Ni(n, γ) reaction acts as a bottleneck when relying on one-zone nucleosynthesis calculations. However, the impact of this reaction is strongly dampened in multizone models of low-metallicity AGB stars experiencing *i*-process nucleosynthesis.

DOI: 10.1103/PhysRevC.111.015803

I. INTRODUCTION

The origin and production mechanism of the heavy elements has been under investigation for a long time. The first direct observations of nucleosynthesis of heavy elements was reported by P. Merrill in 1952 [1]. Soon after, the mechanism behind the production of heavy elements through neutron capture was outlined in the famous B^{2}FH paper in 1957 [2].

Nucleosynthesis beyond the Fe/Ni mass region is due to slow neutron capture (*s* process), rapid neutron capture (*r* process), photodisintegration processes, and more recent results call for an intermediate neutron capture process (*i* process) [3,4]. These processes are sensitive to nuclear properties such as the nuclear level densities (NLD) and γ-ray strength functions (γSF). The availability and uncertainties in nuclear data affect the ability to reliably calculate reaction rates, in particular for the *r* and *i* processes as they involve neutron-rich nuclei for which data are nonexistent or at the very least sparse. This

*Contact author: vetlewi@fys.uio.no
†Contact author: sunniva.siem@fys.uio.no
‡Present address: Department of Physics, University of Liverpool, L69 7ZE, United Kingdom.
§Present address: Departamento de Estructura de la Materia, Física Térmica y Electrónica and IPARCOS, Universidad Complutense de Madrid, E-28040 Madrid, Spain.
‖Present address: Department of Physics, University of Johannesburg, P.O. Box 524, Auckland Park 2006, South Africa.

Published by the American Physical Society under the terms of the Creative Commons Attribution 4.0 International license. Further distribution of this work must maintain attribution to the author(s) and the published article's title, journal citation, and DOI. Open access publication funded by CERN.

can have a significant impact on the neutron capture rates and on the final abundance distribution of elements and their isotopes predicted by models. Currently, the vast majority of nuclei for which NLDs and γSFs have been measured lie at, or are very near, the line of stability [5]. Experimentally measured NLD and γSF can provide significant constraints on calculated neutron capture rates which are relevant for nucleosynthesis models [6,7].

Away from stability, directly measured (n, γ) cross sections are not available and NLDs and γSFs can provide the necessary constraints. The Oslo method is particularly suitable as it extracts NLD and γSF simultaneously [8,9]. These quantities, together with the optical model potentials, are the main ingredients of the *Hauser-Feshbach* theory [10] to calculate neutron capture cross sections and reaction rates. The Oslo method has been extended to include total absorption spectroscopy following β decay leading to the β-Oslo method [11] and has demonstrated the versatility of the Oslo method and its applicability even for nuclei far from stability [11–15]. The β-Oslo method requires specific β-Q value conditions for the mother-daughter pair, placing a limit on the nuclei which can be measured with this technique.

Another approach is to use inverse kinematics with radioactive beams. Here the beam intensity is the main limiting factor. Applying the Oslo method to experimental data from an inverse kinematics experiment was first demonstrated in Ref. [16] extracting the NLD and γSF of ^{87}Kr following a $d(^{86}\text{Kr}, p)^{87}\text{Kr}$ pick-up reaction. In this paper, we have applied this inverse-Oslo method to data from a radioactive ion beam experiment to extract the NLD and γSF of ^{67}Ni. Based on these results, the neutron capture rate of ^{66}Ni was constrained using the Hauser-Feshbach theory, which is of particular importance for our understanding of the weak i process. In the weak i process the neutron density is large ($\sim 10^{15}$), but exposure is low due to a quick and abrupt termination of the neutron production. In such a case only the first n-capture peak elements are produced significantly [17]. This was studied in Ref. [17], where it was found that the $^{66}\text{Ni}(n, \gamma)$ reaction has a major impact on the overall production rate of heavier elements, essentially acting as a bottleneck for the entire weak i process. Constraining the $^{66}\text{Ni}(n, \gamma)$ reaction could improve our understanding of the i-process nucleosynthesis.

II. EXPERIMENT AND ANALYSIS

The experiment was performed using the HIE-ISOLDE facility at CERN [18], where a 1.4-GeV proton beam from the PSBooster bombarded a uranium carbide target inducing fission. The evaporated fission products were ionized by the resonance ionization laser ion source (RILIS) [19] and the ^{66}Ni ions were separated by the General Purpose Separator (GPS) to be collected and cooled by a penning trap (REXTRAP) [20]. The ions were then charge bread to a 16^+ charge state by an electron-beam ion source (REXEBIS) [21,22]. The highly ionized ^{66}Ni ions were reaccelerated by the HIE-ISOLDE linear accelerator to an energy of 4.47(1) MeV/u. The $\approx 3.5 \times 10^6$ pps intense ^{66}Ni beam impinged on a $\approx$670-μg/cm^2-thick secondary deuterated polyethylene target (99% enrichment in deuterium) [23] placed at the Miniball experimental station and produced the desired $d(^{66}\text{Ni}, p)^{67}\text{Ni}$ reactions. The total time of beam on target was approximately 140 h. The same reaction has previously been measured at ISOLDE by Ref. [24], but at a much lower beam energy of 2.5 MeV/u. That data set was not considered as it only reached excitation energies up to 3.5 MeV, much less than what is required for the Oslo method.

TABLE I. Positioning of the γ-ray detectors in the experimental setup.

Detector	ϕ (deg)	θ (deg)	Target distance (cm)
$LaBr_3$:Ce 1	136	147	25
$LaBr_3$:Ce 2	184	147	25
$LaBr_3$:Ce 3	210	147	25
$LaBr_3$:Ce 4	32	64	25
$LaBr_3$:Ce 5	358	64	25
$LaBr_3$:Ce 6	330	64	25
Miniball 1	148	64	12
Miniball 2	228	64	12
Miniball 3	188	101	12
Miniball 4	358	101	12
Miniball 5	312	56	12
Miniball 6	32	56	12

Protons from the reaction were measured with the C-REX particle detector array [25,26], while coincident γ rays were measured using the Miniball detector array [27,28]. Only the downstream particle array was considered due to low yields in the upstream array. The particle detectors considered covered angles between 25° and 49° in the laboratory frame (CM angles 40° to 76°). Two of the eight Miniball high-purity germanium (HPGe) clusters [28] were replaced by six large-volume (3.5 × 8 inch) $LaBr_3$:Ce detectors to increase the high γ-ray energy efficiency of the array. The placement of each detector is given in Table I. Signals from the C-REX detectors were processed by an analog data acquisition system (DAQ) which fed four 32-channel analog-to-digital converter (ADC) modules from Mesytec. The signals from the γ-ray detectors were processed by a digital DAQ consisting of XIA Digital Gamma Finders (DGF-4C). The two systems were synchronized, read out simultaneously, and the data written to disk.

Prompt particle-γ coincidences were selected from the data by applying time gates on the time difference between the detected γ rays and particles, while the (d, p) reaction was selected by applying the appropriate energy cut on the $\Delta E - E$ matrix. Background events were selected in a similar fashion by placing time gates of half the size as the prompt gate on either sides of the prompt peak. This resulted in a total of 3.2×10^5 and 1.1×10^6 background subtracted proton-γ coincidences with the $LaBr_3$:Ce detectors and the Miniball clusters, respectively. The low number of proton-γ coincidences with the $LaBr_3$:Ce compared to those with the Miniball detectors is due to the lower geometric efficiency of the $LaBr_3$:Ce detectors which were located considerably further from the target. Despite having only a quarter of the Miniball coincidences, the more efficient $LaBr_3$:Ce detectors

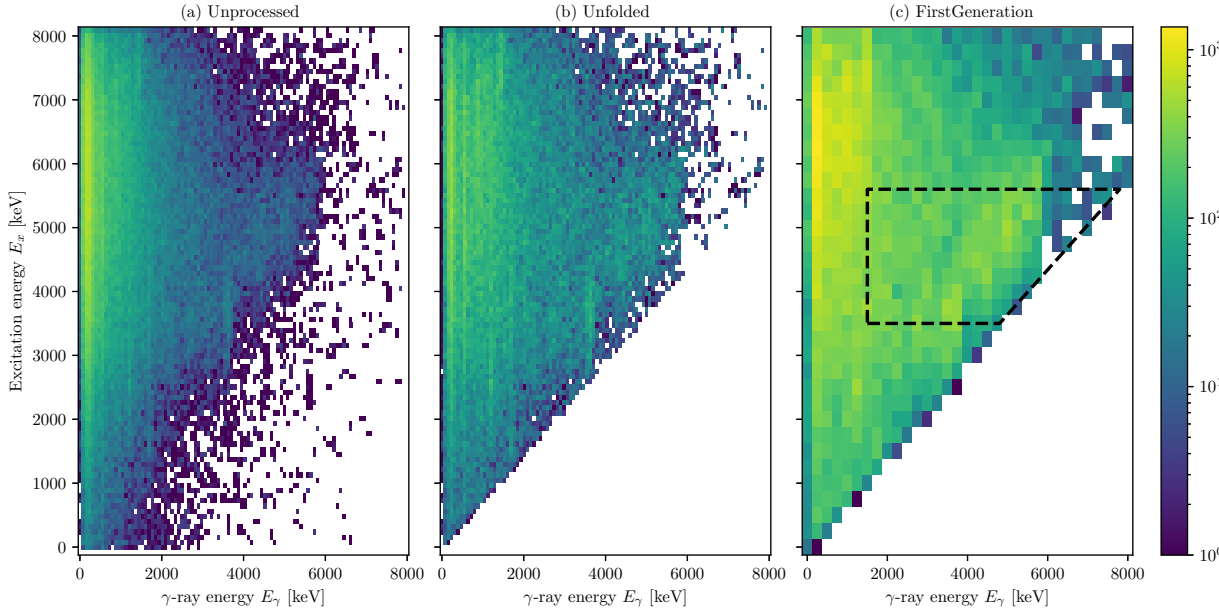


FIG. 1. (a) Unprocessed excitation-γ coincidence and (b) unfolded matrices with 80 keV/bin on both axes. The first-generation matrix (c) was rebinned from 80 to 250 keV/bin to reduce fluctuations. The dashed lines in (c) indicate the region for which the NLD and γSF are extracted.

measured the majority of high-energy γ-ray transitions. For this reason, the results presented here are based on the analysis of proton-γ coincident events from the $LaBr_3$:Ce detectors only.

Due to the considerable residual kinetic energy of ^{67}Ni the γ-ray energies were Doppler corrected. The maximum deflection of the residual ^{67}Ni was less than 1.5° and the maximum spread in velocity was less than 4.2%. The correction was performed using a constant factor based only on the γ-detector angle relative to the beam axis.

For each proton-γ event the excitation energy was calculated from the kinematic reconstruction of the two-body reaction. The proton-γ coincidences were collected in an excitation-γ energy matrix shown in Fig. 1(a). Due to the Lorentz boost associated with inverse-kinematics there were no well-resolved levels in the particle spectra suitable for an in-beam calibration and the FWHM of the excitation energy was ≈1.1 MeV.

The first step to obtain NLDs and γSFs from excitation-γ matrices is to correct for the detector response using the unfolding method [29] by using a detector response deduced from a `Geant4` [30] simulation of the experimental setup [31]. This resulted in the *unfolded* matrix shown in Fig. 1(b).

Next, an iterative subtraction method [32] is applied to the unfolded matrix in order to deduce the distribution of primary γ rays emitted from each excitation bin, resulting in the *first generation* matrix shown in Fig. 1(c).

The first-generation matrix is proportional to the γ-ray transmission coefficients $\mathcal{T}(E_\gamma)$ and the NLD $\rho(E_f = E_x - E_\gamma)$ at the final excitation energy E_f following the first γ decay of the cascade [8]

$$\Gamma(E_x, E_\gamma) \propto \mathcal{T}(E_\gamma)\rho(E_f = E_x - E_\gamma). \tag{1}$$

The NLD and transmission coefficients are extracted by normalizing the first-generation γ-ray spectra for each excitation bin and by fitting the experimental matrix ($\Gamma(E_\gamma, E_x)$) with a theoretical matrix [8]

$$\Gamma_{\rm th}(E_x, E_\gamma) = \frac{\mathcal{T}(E_\gamma)\rho(E_x - E_\gamma)}{\sum_{E_\gamma = E_\gamma^{\rm min}}^{E_x} \mathcal{T}(E_\gamma)\rho(E_x - E_\gamma)} \tag{2}$$

by minimizing

$$\chi^2 = \sum_{E_x, E_\gamma} \left(\frac{\Gamma(E_\gamma, E_x) - \Gamma_{\rm th}(E_\gamma, E_x)}{\Delta\Gamma(E_\gamma, E_x)} \right)^2, \tag{3}$$

where $\mathcal{T}(E_\gamma)$ and $\rho(E_f = E_x - E_\gamma)$ are treated as free parameters for each γ-ray energy E_γ and final energy E_f, respectively. The denominator, $\Delta\Gamma(E_\gamma, E_x)$, represents the experimental uncertainty in the first-generation matrix. Considering the experimental resolution and to ensure that only primary transitions, originating in the quasicontinuum, are considered a minimum γ-ray energy of 1.5 MeV was selected. Similarly, only excitation energy bins between 3.5 and 5.6 MeV were included in the fit. These E_γ and E_x energy regions have been chosen based on the guidelines of Ref. [33].

The resulting γ-ray transmission coefficients are converted to γSF by

$$f(E_\gamma) = \frac{\mathcal{T}(E_\gamma)}{2\pi E_\gamma^3}$$

under the assumption that the transmission coefficients are dominated by dipole transitions.

The theoretical first-generation matrix, Eq. (2), is invariant under transformation of NLD and γSF [8],

$$\widetilde{\rho}(E_f) = A\rho(E_f)e^{\alpha E_f}$$
$$\widetilde{f}(E_\gamma) = Bf(E_\gamma)e^{\alpha E_\gamma}, \tag{4}$$

where A, B, and α are transformation parameters. This means that the extracted NLD and γSF do not represent the physical NLD and γSF but contain information on the functional shape. To deduce the absolute values of the NLD and γSF the extracted NLD and γSF will have to be normalized to auxiliary data.

III. NORMALIZATION OF NLD AND γSF

Many nuclei along the island of stability have auxiliary data available with which the normalization of the NLDs and γSFs is achieved. Typical data used for this purpose are the level density from resolved discrete states, the level density at the neutron separation energy ($S_n = 5.8$ MeV) from s- and/or p-wave neutron resonance spacing data, and the average radiative widths of s-wave neutron resonances. When applying the Oslo method, NLDs do not extend to S_n as the method probes the NLD at the final excitation energy $E_f = E_x^{\max} - E_\gamma$, the maximum energy possible to be considered in the first-generation matrix is $E_x^{\max}$, and is typically the neutron separation energy (depending on reaction kinematics) [33], but in this case slightly below at 5.6 MeV, which corresponds to a final and highest excitation energy of 4.1 MeV. Hence, the measured NLDs are typically interpolated to the NLDs from resonance data at S_n.

The impact on the uncertainty of NLDs and γSF on the availability of neutron resonance data has recently been demonstrated [34]. In the absence of neutron resonance data, the resonance spacing or radiative widths of neutron resonances are generally estimated from systematics of neighboring nuclei, see for instance Refs. [35–37]. Similarly, for β-Oslo measurements various combinations of solutions have been used ranging from systematic information of nearby nuclei [11,38], model calculations [14,38,39], or the shape method [38–41]. Neither for ^{67}Ni nor for surrounding nuclei are neutron resonance data available. The situation is further aggravated by an incomplete level scheme at low excitation energies resulting in an unreliable level density of resolved discrete states which, together with the low experimental resolution, makes the application of the shape method not ideal. With the absence of any reliable normalization points the only practical solution for normalizing the NLD and γSF is the reliance on model estimates.

A. Bayesian analysis

Despite the lack of auxiliary data for normalization it is still possible to constrain the experimental NLD and γSF as the true values are expected to fall within the range of commonly accepted models. For example, the NLD in statistical nuclei grows exponentially and are often well reproduced by large shell-model calculations [12,42] at low energies and the constant temperature [43], back-shifted Fermi gas [44] or microscopic Hartree-Fock [45] calculations at high energies. Similarly, the γSF is expected to follow the tail of the GDR and typically features resonances such as the upbend and/or a Pygmy dipole resonance (PDR). This is typically well described by the phenomenological simple modified Lorentzian model (SMLO) or the microscopic mean field plus quasiparticle random-phase approximation both of which being the recommended global models to describe the γSF [5]. By assuming a combination of NLD and γSF models one can constrain the possible values for the normalization parameters, A, B and α in Eq. (4).

TABLE II. List of all NLD and γSF models considered together with their parameters. The $E1$ strength for the γSF is model by either by SMLO ($E1$) or HFB-QRPA ($E1$), while the $M1$ strength parameters are referred to as $M1$. The PDR feature seen in ^{68}Ni was modeled as $E1$ with the parameters denoted as PDR.

	Model	Parameters
$\boldsymbol{\theta}_{\text{NLD}}$	CT	T, δ_{CT}, σ_d, $\sigma(S_n)$
	BSFG	a, δ_{BSFG}, σ_d, $\sigma(S_n)$
	HFB	c, δ_{HFB}
$\boldsymbol{\theta}_{\gamma\text{SF}}$	SMLO ($E1$)	E_{GDR}, Γ_{GDR}, σ_{GDR}
	HFB-QRPA ($E1$)	c_{E1}, δ_{E1}, f_0, ϵ_0, U
	PDR ($E1$)	E_{PDR}, Γ_{PDR}, σ_{PDR}
	$M1$	E_{sf}, Γ_{sf}, σ_{sf}, C, η

This can be taken a step further by considering several models for NLD and γSF to get a range of acceptable normalization parameters. To perform such an analysis we apply Bayesian statistics. Analyzing Oslo method data within a Bayesian statistics framework has previously been demonstrated by Midtbø *et al.* [9] and our analysis is based on the framework presented therein. The starting point of the normalization analysis is Bayes's theorem

$$P(\boldsymbol{\theta}|\{\rho_i\},\{f_i\}) = \frac{\mathcal{L}(\{\rho_i\},\{f_i\}|\boldsymbol{\theta})P(\boldsymbol{\theta})}{P(\{\rho_i\},\{f_i\})}, \tag{5}$$

where $P(\boldsymbol{\theta}|\{\rho_i\},\{f_i\})$ is the posterior probability of a set of normalization and model parameters $\boldsymbol{\theta} = (A, B, \alpha, \boldsymbol{\theta}_{\text{NLD}}, \boldsymbol{\theta}_{\gamma\text{SF}})$, given a set of non-normalized measured NLD points $\{\rho_i\}$ and γSF points $\{f_i\}$. The likelihood $\mathcal{L}(\{\rho_i\},\{f_i\}|\boldsymbol{\theta})$ is the probability of measuring non-normalized NLD and γSF given the set of parameters $\boldsymbol{\theta}$. $P(\boldsymbol{\theta})$ is the prior probability of a set of normalization and model parameters. The prior will be further discussed in Sec. III C, while the physical models and their parameters are presented in Sec. III B and summarized in Table II. The evidence $P(\{\rho_i\},\{f_i\})$ is the probability of measuring the non-normalized NLD and γSF, and can be treated as a normalization factor. With the assumption of Gaussian distributed uncertainties of the measured non-normalized NLD and γSF leads to the likelihood

$$\mathcal{L}(\boldsymbol{\theta}) = \prod_i \mathcal{L}_i(\boldsymbol{\theta}), \tag{6}$$

with $\mathcal{L}_i(\boldsymbol{\theta})$ corresponding to

$$\ln \mathcal{L}_{\text{discrete}} = \sum_j \ln \frac{1}{\sqrt{2\pi}\sigma_{\rho_j,\text{Oslo}}(\boldsymbol{\theta})} - \frac{1}{2}\sum_j \left(\frac{\rho_{j,\text{discrete}} - \rho_{j,\text{Oslo}}(\boldsymbol{\theta})}{\sigma_{\rho_j,\text{Oslo}}(\boldsymbol{\theta})}\right)^2, \quad (7)$$

$$\ln \mathcal{L}_{\text{NLD}} = \sum_j \ln \frac{1}{\sqrt{2\pi}\sigma_{\rho_j,\text{Oslo}}(\boldsymbol{\theta})} - \frac{1}{2}\sum_j \left(\frac{\rho_{j,\text{model}}(\boldsymbol{\theta}) - \rho_{j,\text{Oslo}}(\boldsymbol{\theta})}{\sigma_{\rho_j,\text{Oslo}}(\boldsymbol{\theta})}\right)^2, \quad (8)$$

$$\ln \mathcal{L}_{\gamma\text{SF}} = \sum_j \ln \frac{1}{\sqrt{2\pi}\sigma_{f_j,\text{Oslo}}(\boldsymbol{\theta})} - \frac{1}{2}\sum_j \left(\frac{f_{j,\text{model}}(\boldsymbol{\theta}) - f_{j,\text{Oslo}}(\boldsymbol{\theta})}{\sigma_{f_j,\text{Oslo}}(\boldsymbol{\theta})}\right)^2, \quad (9)$$

$$\ln \mathcal{L}_{^{68}\text{Ni}} = \sum_j \ln \frac{1}{\sqrt{2\pi}\sigma_{j,^{68}\text{Ni}}} \quad (10)$$

$$-\frac{1}{2}\sum_j \left(\frac{f_{j,\text{model}}(\boldsymbol{\theta}) - f_{j,^{68}\text{Ni}}(\boldsymbol{\theta})}{\sigma_{j,^{68}\text{Ni}}}\right)^2. \quad (11)$$

Here $\mathcal{L}_{\text{discrete}}$ represents the likelihood of measuring a set of NLDs given the known level density from discrete levels $\rho_{j,\text{discrete}}$, $\mathcal{L}_{\text{NLD}}$ is the likelihood given a specific NLD model and $\mathcal{L}_{\gamma\text{SF}}$ is the likelihood given a γSF model. The NLD between excitation energies between 1.0 and 2.4 MeV are considered in Eq. (7) while NLD between 2.6 and 3.8 MeV are considered in Eq. (8). All measured γSF energies are included in Eq. (9). The $\mathcal{L}_{^{68}\text{Ni}}$ likelihood is included to further constrain the γSF using the measured γSF in ^{68}Ni as the γSF above the neutron separation energy are typically very similar in neighboring nuclei. $\rho_{j,\text{Oslo}}(\boldsymbol{\theta})$, $(f_{j,\text{Oslo}}(\boldsymbol{\theta}))$, and $\sigma_{\rho_j,\text{Oslo}}((\boldsymbol{\theta})$ $(\sigma_{f_j,\text{Oslo}}(\boldsymbol{\theta}))$ are the normalized NLD (γSF) and standard deviation, given a set of normalization parameters $A, B, \alpha \in \boldsymbol{\theta}$, respectively, see Eq. (4).

Instead of NLDs from resolved discrete states we have considered level densities based on the counting of levels from large-scale shell-model (SM) calculations utilizing the `ca48mh1g` interaction, see Refs. [12,46] for details.

To perform the actual Bayesian analysis, model and normalization parameters were sampled using the Bayesian nested sampling algorithm `MultiNest` [47–49] in the `PyMultiNest` package [50] to obtain a posterior probability distributions of the normalization and model parameters $\boldsymbol{\theta}$, given as samples $\boldsymbol{\theta}_i$.

B. Models

A total of three NLD models and four γSF models have been considered, making the total number of inferred posteriors twelve. In this section we will describe the models considered.

NLD

For energies above the point where the model space of the shell-model calculation is exhausted the NLD has been modeled with three different models. These include the back-shifted Fermi gas (BSFG) model [51,52]

$$\rho_{\text{BSFG}}(E_x) = \frac{\sqrt{\pi}}{12\sigma}\frac{\exp(2\sqrt{a(E_x-\delta)})}{a^{1/4}(E_x-\delta)^{5/4}}, \quad (12)$$

where a is the level density parameter, δ is the energy shift, and σ is the spin-cutoff parameter. The constant temperature (CT) model [53]

$$\rho_{\text{CT}}(E_x) = \frac{1}{T}e^{\frac{E_x-\delta}{T}}, \quad (13)$$

where T is the nuclear temperature and δ is an energy shift parameter. Last, tabulated Hartree-Fock-Bogoliubov (HFB) calculations [54] were also considered and allowed to be renormalized through

$$\rho_{\text{HFB}}(E_x) = \hat{\rho}_{\text{HFB}}(E_x-\delta)e^{c\sqrt{E_x-\delta}}, \quad (14)$$

where again δ is used to denote an energy shift, c is a slope parameter, and $\hat{\rho}_{\text{HFB}}$ are the tabulated NLDs. It should be noted that δ in Eqs. (12), (13), and (14) are not the same parameters and will be subscripted whenever there is ambiguity which parameter is being referenced. The spin distribution for the BSFG and CT models was given by the Bethe/Ericson distribution [51,53]

$$g(E_x, J) = \exp\left(-\frac{J^2}{2\sigma^2(E_x)}\right) - \exp\left(-\frac{(J+1)^2}{2\sigma^2(E_x)}\right), \quad (15)$$

with the spin-cutoff parameterized by [55,56]

$$\sigma^2(E_x) = \begin{cases} \sigma_d^2 & E < E_d \\ \sigma_d^2 + \frac{E-E_d}{S_n-E_d}\left(\sigma^2(S_n) - \sigma_d^2\right) & E \geqslant E_d, \end{cases} \quad (16)$$

where σ_d is the discrete spin-cutoff parameter, obtained from shell-model result as discussed in Sec. III C, with a constant spin distribution at energies below $E_d = 2.0$ MeV.

γSF

For the γSF we have considered the SMLO [57] and the microscopic Gogny-HFB plus quasiparticle random-phase approximation (Gogny-HFB + QRPA) with phenomenological corrections [58], which are the recommended global models for the γSF [5]. The SMLO model describes the $E1$ γSF with the giant dipole resonance (GDR) for photoemission strength and is given by

$$f_{\text{GDR}}(E_\gamma) = \frac{1}{3\pi^2\hbar^2c^2}\frac{\sigma_{\text{TRK}}}{1-\exp(-E_\gamma/T)} \times \frac{2}{\pi}\frac{E_\gamma\Gamma(E_\gamma,T)}{\left(E_\gamma^2 - E_{\text{GDR}}^2\right)^2 + E_\gamma^2\Gamma^2(E_\gamma,T)}, \quad (17)$$

where E_{GDR} is the centroid of the GDR, $\sigma_{\text{TRK}} = 60\frac{NZ}{A}$ is the Thomas-Reiche-Kuhn sum rule [57], and T is the temperature at the final excitation energy. The width,

$$\Gamma(E_\gamma, T) = \frac{\Gamma_{\text{GDR}}}{E_{\text{GDR}}}\left(E_\gamma + \frac{(2\pi T)^2}{E_{\text{GDR}}}\right), \quad (18)$$

depends on the final temperature and the $\Gamma_{\rm GDR}$ which is the width found in the photoabsorption strength function. Within the SMLO model the $M1$ strength is parameterized as two standard Lorentzians (SLO)

$$f_{\rm SLO}(E_\gamma) = \frac{1}{3\pi^2\hbar^2c^2}\frac{E_\gamma\Gamma^2}{\left(E_\gamma^2 - E_r^2\right)^2 + (E_\gamma\Gamma)^2} \quad (19)$$

for the scissors and the spin-flip resonances. The low-energy upbend is modeled as a simple exponential [54]. From the shape of the non-normalized γSF there are no obvious signs of a scissors resonance which is consistent with the relatively low estimated axial deformation of $\beta_2 = 0.05$ [59] and has been omitted from further consideration in the model for the γSF. The assumed $M1$ strength contributions are thus

$$f_{\rm M1}(E_\gamma) = f_{\rm SLO}(E_\gamma, E_{\rm sf}, \Gamma_{\rm sf}, \sigma_{\rm sf}) + C\exp(-\eta E_\gamma), \quad (20)$$

where $E_{\rm sf}$ is the mean energy, $\Gamma_{\rm sf}$ is the width, and $\sigma_{\rm sf}$ the cross section of the spin-flip resonance. The parameters of the upbend, η and C have no physical interpretation and are treated as free parameters chosen to best describe the shape of the upbend. The assumption for the $M1$ multipolarity of the upbend is based on results from shell-model calculations [42,60–62] and from a measurement albeit not conclusively [63].

In the Gogny-HFB + QRPA model, the photoemission $E1$ strength is given by

$$f_{E1}(E_\gamma) = c_{E1}f_{E1}^{\rm QRPA}(E_\gamma - \delta_{E1}) + \frac{f_0 U}{1+\exp(E_\gamma - \epsilon_0)}, \quad (21)$$

where $f_{E1}^{\rm QRPA}(E_\gamma)$ is the strength found in Gogny-HFB + QRPA calculations. The phenomenological parameters f_0, ϵ_0 are free parameters, and U is the excitation energy of the initial level. The strength is allowed to be scaled and shifted through the free parameters c_{E1} and δ_{E1}, respectively. The $M1$ strength was estimated within the SMLO model, Eq. (20).

Data points from a Coulomb dissociation measurement of ^{68}Ni are also considered [64]. This features a strong narrow PDR at $E_x \approx 9.5$ MeV which has been accounted for by including a SLO in the $E1$ strength. Since the extracted γSF in ^{67}Ni only extends to 5.5 MeV we cannot determine if such a PDR also exists in ^{67}Ni. In order to account for either possibility, we have repeated the analysis both with and without including the PDR, observed in ^{68}Ni, in the ^{67}Ni strength. In the latter case, the two experimental points at $E_\gamma = 8.4$ MeV and $E_\gamma = 9.5$ MeV of ^{68}Ni were excluded and removed from consideration in Eq. (11). A list of all model combinations and their parameters are listed in Table II.

C. Parameter priors

For all model parameters, the probability distribution were assumed to be Gaussian or truncated Gaussian probability density functions (PDF). The latter used for parameters where there are physical justifications for why the values cannot have certain values (e.g. no negative temperature).

The normalization parameters required to transform the NLD and γSF to the physical solution are arbitrary and we have no a priori knowledge other than that A and B has to be positive. Ideally, flat prior probability distributions should be used for A, B and α, with the former two truncated to positive values. However, this is computationally expensive. Instead truncated Gaussian distributions were used for A and B and a Gaussian probability distribution for α. To maintain an uninformed prior the standard deviation of the probability distribution for A and B were set to 10 times the centroid, while the standard deviation of the prior probability distribution of α was set to 1 1/MeV. The latter was chosen due to the high sensitivity of the likelihood to this parameter. The centroid of the prior probability distributions were selected to be the A, B and α values that maximized the likelihood Eq. (6). Numerical values for the centroids of A, B and α PDFs are in the Supplemental Material [65].

TABLE III. Model parameter priors used for the extrapolation of the NLD between the experimental points and the neutron separation energy. The last column indicates whether a Gaussian ($\mathcal{N}$) or truncated Gaussian ($\mathcal{N}_t$) PDF are used as the prior probability distribution.

Parameter	μ	σ	PDF
a	8.2 MeV	8.2 MeV	$\mathcal{N}_t$
δ (BSFG)	0 MeV	10 MeV	$\mathcal{N}$
T	0.958 MeV	2 MeV	$\mathcal{N}_t$
δ (CT)	−0.359 MeV	10 MeV	$\mathcal{N}$
c (HFB)	0 MeV$^{-1/2}$	1 MeV$^{-1/2}$	$\mathcal{N}$
δ (HFB)	0 MeV	1 MeV	$\mathcal{N}$
σ_d	2.5	0.25	$\mathcal{N}_t$
$\sigma(S_n)$	3.8	0.38	$\mathcal{N}_t$

For the NLD models fairly weak informed priors were used. In the case of the BSFG model the level density parameter a mean value of $\mu = 8.2$ MeV was selected as the approximate mean of the systematics from Refs. [52,66], Refs. [67,68] and Ref. [68] with width $\sigma = \mu$. The shift parameter $\delta_{\rm BSFG}$ is a Gaussian with $\mu = 0$ MeV and $\sigma = 10$ MeV. Similarly the CT model priors were selected from the systematics of Ref. [68] with widths of $\sigma = 2$ MeV for the temperature and $\sigma = 10$ MeV for the shift parameter $\delta_{\rm CT}$. The slope and shift parameters c and $\delta_{\rm HFB}$ for the HFB was centered around 0 MeV$^{-1/2}$ and 0 MeV with widths of 1 MeV$^{-1/2}$ and 1 MeV, respectively. The discrete spin-cutoff parameter from Eq. (16) was found to be $\sigma_d = 2.50(25)$ by examining the tabulated shell-model levels while the spin-cutoff at the neutron separation energy is $\sigma(S_n) = 3.80(38)$ from an average of spin-cut off models in Refs. [52,54,67]. In both cases an uncertainty of 10% was assumed. The priors for all NLD model parameters are listed in Table III.

The parameters for the SMLO model were taken from the systematics in Ref. [57]. Unless an uncertainty was provided it was assumed to be 10%. The scale c_{E1} and shift δ_{E1} for the Gogny-HFB + QRPA was assumed to be centered around 1 and 0 MeV, respectively, with a width of 0.5 MeV for both. The phenomenological parameters f_0 and ϵ_0 are taken from [58], while the probability distribution of the initial excitation energy U was modeled as a truncated Gaussian at the excitation range used to extract the NLD and γSF (3.5 and

TABLE IV. Model parameter priors used for the γSF models extrapolated to the extracted γSF of ^{67}Ni. The last column indicates whether a Gaussian ($\mathcal{N}$) or truncated Gaussian ($\mathcal{N}_t$) PDF are used as the prior probability distribution.

Parameter	μ	σ	PDF
E_{GDR}	17.68 MeV	0.19 MeV	$\mathcal{N}_t$
Γ_{GDR}	6.0 MeV	2.8 MeV	$\mathcal{N}_t$
σ_{GDR}	978 mb	98 mb	$\mathcal{N}_t$
c_{E1}	1	0.5	$\mathcal{N}_t$
δ_{E1}	0 MeV	0.5 MeV	$\mathcal{N}$
f_0	2.5×10^{-10} MeV^{-4}	2.5×10^{-10} MeV^{-4}	$\mathcal{N}_t$
ϵ_0	4 MeV	1 MeV	$\mathcal{N}$
U	4.45 MeV	1.1 MeV	$\mathcal{N}_t$
E_{PDR}	9.55 MeV	0.17 MeV	$\mathcal{N}_t$
Γ_{PDR}	1.02	0.26 MeV	$\mathcal{N}_t$
σ_{PDR}	27.4 mb	5.6 mb	$\mathcal{N}_t$
E_{sf}	8.93 MeV	0.90 MeV	$\mathcal{N}_t$
Γ_{sf}	4.0 MeV	0.4 MeV	$\mathcal{N}_t$
σ_{sf}	1.0 mb	0.1 mb	$\mathcal{N}_t$
C	3.5×10^{-8} MeV^{-3}	3.5×10^{-8} MeV^{-3}	$\mathcal{N}_t$
η	0.8 1/MeV	0.08 1/MeV	$\mathcal{N}$

5.6 MeV) with a mean of 4.5 MeV and a standard deviation of 1.1 MeV. The spin-flip and upbend parameters were taken from Ref. [57] assuming 10% uncertainty, except for C, where the width was assumed to be the same as the mean. Last, the PDR parameters were taken from Ref. [64]. All priors parameters related to the γSF models are listed in Table IV.

D. Hauser-Feshbach calculations and results

For each sample $\boldsymbol{\theta}_i$ the normalized NLD and γSF are calculated and the marginal posterior probability distribution for each NLD and γSF point is obtained for each combination of NLD and γSF models. Weighting each combination of models equally, the average normalized NLD and γSF are shown in Figs. 2 and 3, respectively. The 68, 95, and 99.7% credibility intervals (1, 2, and 3 standard deviations) of the model predictions are found by calculating the NLD and γSF for each sample $\boldsymbol{\theta}_i$ and weighting each combination of models equally. The posterior mean values for all model and normalization parameters are in the Supplemental Material [65]. The impact of including the PDR structure in the models for the γSF reported in Ref. [64] is shown in Fig. 4 to be negligible for the normalization of the γSF. The NLD at the neutron separation energy is found to be $1.22(51) \times 10^3$ MeV^{-1} by averaging the NLD models.

The measured NLD and γSF in ^{67}Ni were used in Hauser-Feshbach calculations to constrain the neutron capture cross section of ^{66}Ni. From each posterior sample $\boldsymbol{\theta}_i$ of normalization and model parameters tabulated NLD and γSF values were generated from linear interpolation and used as input to the TALYS[1] reaction code [71]. Since the level scheme of ^{67}Ni is far from complete only the first two discrete levels were

[1]Version 1.96.

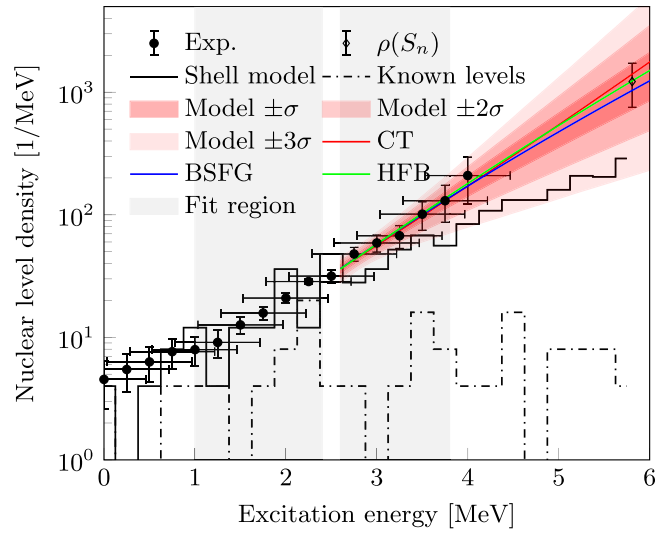


FIG. 2. The measured nuclear level density of ^{67}Ni is shown by the black circles while the black line shows the NLD from large-scale SM calculations [46]. The black dash-dotted line shows the NLD from known discrete levels [69,70]. The red, blue, and green lines show the average for the CT, BSFG, and HFB models, respectively. The red-shaded area indicates the $\pm1\sigma$, $\pm2\sigma$, and $\pm3\sigma$ credibility intervals. The black open diamond represents the extrapolated NLD at the neutron separation energy. The gray-shaded areas indicate the fitting regions to the discrete levels (lower energy) and to the extrapolated models normalized to the measured NLD (higher energy).

included in the Hauser-Feshbach calculations, while above those the provided tabulated NLD was used. Each realization of the capture cross section and reaction rate is weighted equally to obtain a mean cross section and reaction rate and the credibility bands shown in Figs. 5 and 6. The impact of the optical model potential (OMP) has been tested by performing calculations with the phenomenological OMP of Ref. [77] and the microscopic OMP of Ref. [78] and found to have a negligible contribution to the uncertainty.

In the sensitivity study of Ref. [17] the ^{66}Ni(n,γ) reaction rates were taken from the JINA REACLIB v1.1 library [75], indicated by the red dashed line in Fig. 6. The maximum and minimum reaction rates considered by Ref. [17] are based on the models listed in Table 1 of Ref. [79], and these results have been reproduced as indicated by the red band in Figs. 5 and 6. For comparison, the capture cross section and rate with the default selection of NLD (CT+Fermi-Gas), γSF (SMLO [57]+LEE) models, and optical model potential (local phenomenological OMP) in TALYS version 1.96 are shown by the black dashed lines in Figs. 5 and 6.

IV. DISCUSSION

The Oslo method relies on external nuclear data for the normalization. In the absence of those, additional uncertainties may be induced and model dependencies may become significant. This is apparent through the relatively large uncertainties toward S_n on the measured NLD for ^{67}Ni.

The challenge specific to inverse kinematic reactions is the Lorentz boost which causes a strong angular dependence in

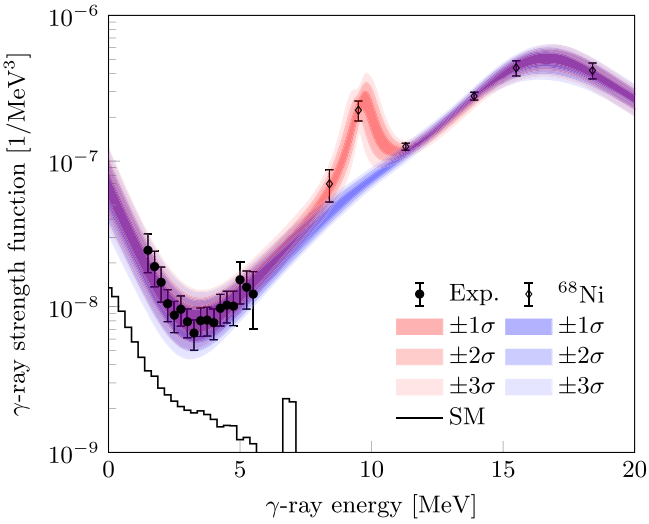


FIG. 3. The measured γ-ray strength function of ^{67}Ni is shown by the black circles while the black line shows the $M1$ strength found in large-scale SM calculations from Ref. [46]. The red- and blue-shaded area indicates the $\pm1\sigma$, $\pm2\sigma$, and $\pm3\sigma$ credibility intervals for the models including the PDR and the models excluding the PDR, respectively. The black open diamonds are the γSF data of ^{68}Ni measured by Rossi *et al.* [64].

the kinematic reconstruction of the residual excitation energy. This leads to an excitation-energy resolution which is limited by the angular opening of the particle telescope's active areas. The consequences are most apparent in the NLD where very little structures are visible.

In contrast, the measured γSF still retains noticeable features and clearly exhibits a well established enhancement for $E_x < 4$ MeV similar to those found in other Ni isotopes [12,34,44,80–82]. Its observation indicates that the upbend is a structure which exists also away from stability. The upbend

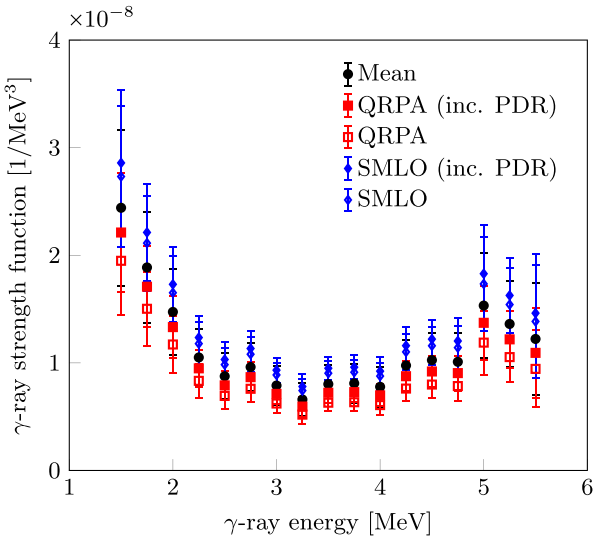


FIG. 4. Comparison of the various γSF normalizations including and excluding the PDR. The black circles show the average normalized γSF.

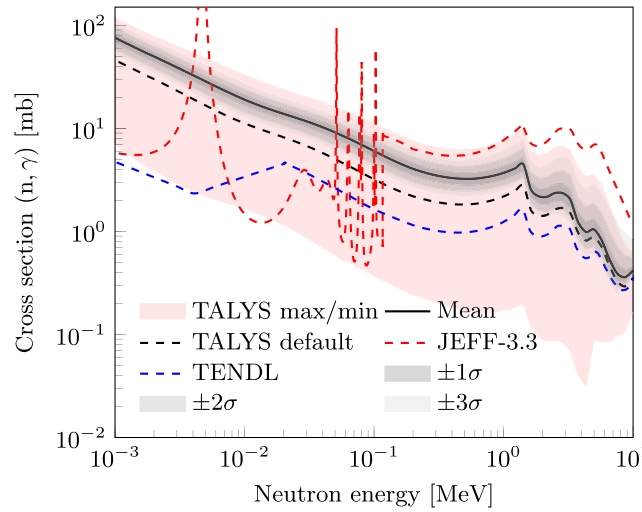


FIG. 5. The mean calculated capture cross section from the sampled NLD and γSF are given by the black line. The gray-shaded area shows the $\pm1\sigma$, $\pm2\sigma$, and $\pm3\sigma$ credibility intervals. The black dashed line represents the capture cross section with TALYS default models (CT/Fermi-Gas + SMLO). The red-shaded area shows the maximum and minimum limits based on calculations using the same NLD and γSF model combinations as Ref. [17]. The red and blue dashed lines shows the JEFF-3.3 library [72] and the TENDL library [73], respectively, the former including a set of unobserved resonance added *ad hoc* as explained in Ref. [74].

in ^{67}Ni is predicted to be due to $M1$ strength, based on large-scale shell-model calculations [46], and shown by the black solid line in Fig. 3. The significant strength in the enhancement and the simultaneous absence of a measurable scissors resonance may be supportive of the suggested connection of the two structures [61,83], although results on the γSF in $^{142,144-151}$Nd seem to contradict this [84].

The calculated ^{66}Ni(n,γ) capture cross section in Fig. 5 features an uncertainty of ≈40%, constraining the cross section considerably. It is interesting to note that our cross section, lies consistently higher than the recommended values as provided in TALYS and TENDL but is smaller than those of JEFF 3.3 for $E_n > 100$ keV. These differences highlight the necessity for measurements of NLDs and γSFs, especially for nuclei away from stability.

Reference [17] allows the capture rate to vary within the red band as indicated in Fig. 6, with the nominal value taken from the JINA REACLIB v1.1 database [75]. Our results constrain the capture rate significantly and show that this rate is found at the high end of the range used by Ref. [17]. This suggests a short exposure time for the weak i process and could help pinpoint details in the stellar environment responsible to produce neutrons.

V. ASTROPHYSICAL IMPLICATIONS

The ^{66}Ni(n,γ) capture rate was suggested to be of key importance for the overall production of heavy elements during the i-process nucleosynthesis taking place in

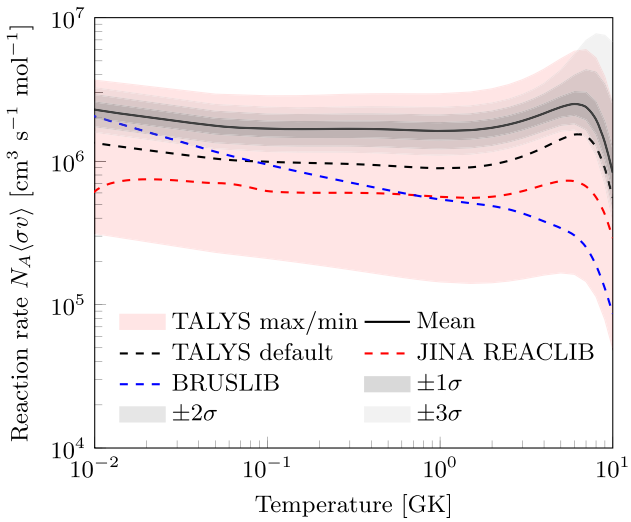


FIG. 6. The mean calculated capture rate from the sampled NLD and γSF are given by the black line. The gray filled area shows the $\pm1\sigma$, $\pm2\sigma$, and $\pm3\sigma$ credibility intervals. The black dashed line is the capture rate with TALYS default (CT/Fermi-Gas + SMLO). The red and blue dashed lines are the reaction rates from JINA REACLIB v1.1 [75] and BRUSLIB [76], respectively. The red-shaded area shows the maximum and minimum limits based on calculations using the same NLD and γSF model combinations as Ref. [17].

Sakurai's object or rapidly accreting white dwarfs [17]. One possible astrophysical site with similar *i*-process conditions are low-metallicity low-mass stars during the early thermally pulsating asymptotic giant branch (AGB) phase [85–89]. During this stage, protons can be engulfed by the convective thermal pulse. As they are transported downward by convection on a timescale of about 1 h, they are burnt rapidly by ^{12}C$(p,\gamma)^{13}$N. After the decay of ^{13}N to ^{13}C in about 10 min, the reaction ^{13}C(α,n) is activated at the bottom of the thermal pulse and leads to neutron densities of up to $\sim10^{15}$ cm^{-3}. Stellar modeling was performed with the stellar evolution code STAREVOL [90–92]. A 1 $M_\odot$ AGB model at a metallicity of [Fe/H] $= -2.5$ is considered. This model is discussed in detail in Ref. [89].

We estimated the impact of the new ^{66}Ni(n,γ) rate on the *i*-process nucleosynthesis in these objects. The effects are evaluated on both multizone stellar evolution models and in one-zone nucleosynthesis calculations. We used a reaction network including 1160 nuclei, linked through 2123 nuclear reactions (n, p, and α captures and α decays) and weak interactions (electron captures, β decays). Nuclear reaction rates were taken from BRUSLIB, the Nuclear Astrophysics Library of the Université Libre de Bruxelles[2] [76] and the updated experimental and theoretical rates from the NETGEN interface [94]. Additional details can be found in Refs. [89,95,96]. In our sensitivity analysis, eight cases were investigated. We consider, for the ^{66}Ni(n,γ) reaction, the recommended Maxwellian-averaged cross section (MACS) from this work (10.7 ± 5 mb at 30 keV) as well as the minimum (1 mb at 30 keV) and maximum (19 mb at 30 keV) rates predicted by a global unconstrained TALYS calculation (i.e. maximum and minimum reaction rates as prescribed in Ref. [17]). Additionally, the rate of ^{65}Ni(n,γ) was also varied because ^{65}Ni has a half-life of $\sim$2.5 h (55 h for ^{66}Ni), which is fast enough to partially bypass the neutron capture during the *i* process. For ^{65}Ni(n,γ), we considered the minimum (10 mb at 30 keV) and maximum (70 mb at 30 keV) MACS predicted by TALYS for different NLD and γSF models. We also considered the uncertainties related to the nominal ^{66}Ni(n,γ) MACS evaluated in this study by varying it by ±5 mb at 30 keV (cases 1B, 1C, 2B, and 2C). The different cases considered are reported in Table V.

TABLE V. The different cases considered for the rates of ^{65}Ni(n,γ) and ^{66}Ni(n,γ) for the one-zone and stellar-model calculations.

	^{65}Ni(n,γ)	^{66}Ni(n,γ)
Case 1	TALYS min	nominal
Case 1B	TALYS min	nominal − 5 mb
Case 1C	TALYS min	nominal + 5 mb
Case 2	TALYS max	nominal
Case 2B	TALYS max	nominal − 5 mb
Case 2C	TALYS max	nominal + 5 mb
Case 3	TALYS max	TALYS min
Case 4	TALYS max	TALYS max

The initial abundances of the one-zone model correspond to the chemical composition in the thermal pulse of the AGB stellar model, just before the start of the proton ingestion event. The temperature and density were fixed to 220 MK and 2500 g cm^{-3}, respectively, which are typical values in the pulse of low-metallicity AGB models. The nucleosynthesis was calculated over a total time of 2×10^5 s ($\sim$2.3 days). To mimic the proton ingestion episode in the one-zone model, an initial abundance of protons was set to 2×10^{-5} and 3×10^{-4} leading to maximum neutron densities of $N_{n,\max}=1.5\times10^{14}$ cm^{-3} and 6.7×10^{14} cm^{-3}, respectively. For a low initial proton abundance, a weak *i* process develops and elements up to the first peak ($A\lesssim90$) are synthesized (Fig. 7, black pattern). With more protons, a larger neutron

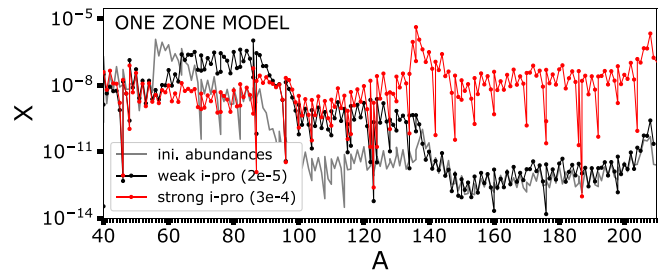


FIG. 7. Final nuclei mass fractions (after decays) as a function of mass number after a weak (black) and a strong (red) *i* process using the one-zone model. The initial proton mass fraction is indicated in parenthesis (see text for details). The gray pattern shows the initial abundances.

[2]Available at [93].

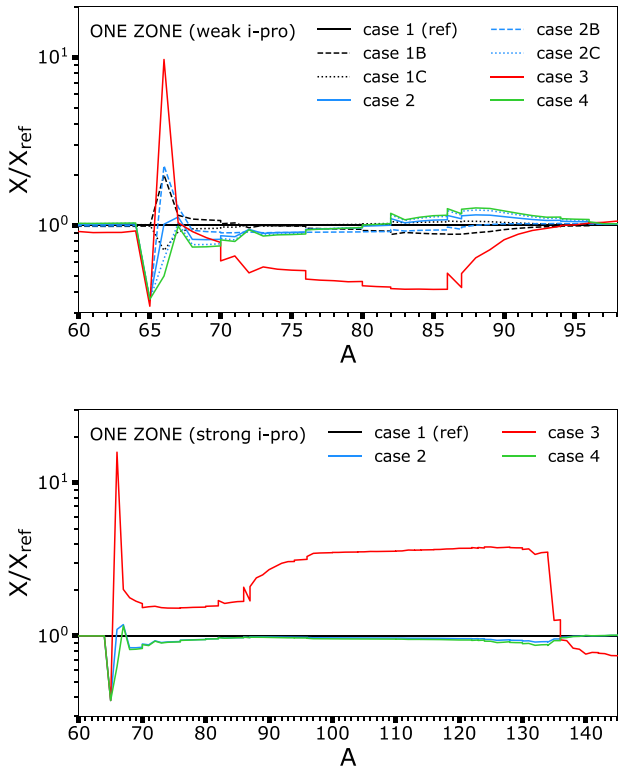


FIG. 8. Final nuclei mass fractions (after decays) as a function of mass number after a weak (top panel) and a strong (bottom) *i* process using the one-zone model. The abundances are normalized by the abundances of the case 1. The eight cases correspond to the eight different combinations of rates indicated in Table V (cases 1B, 1C, 2B, and 2C are not shown in the bottom panel for clarity).

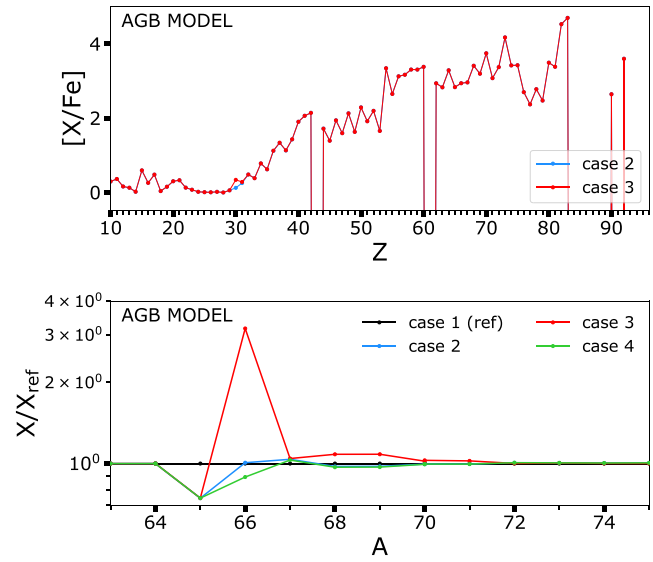


FIG. 9. Final surface abundances (after decays) for a full AGB stellar model. Top: [X/Fe] ratios, defined as $[\mathrm{X/Fe}] = \log_{10}(N_\mathrm{X}/N_\mathrm{Fe})_\star - \log_{10}(N_\mathrm{X}/N_\mathrm{Fe})_\odot$ with N_X the number density of an element X. The first and second $\log_{10}$ terms refer to the abundances of the model and the Sun, respectively. Bottom: same as Fig. 8. The four cases correspond to the four different combinations of rates indicated in Table V.

density is reached and elements of the third peak (Fig. 7, red pattern) are produced. For this particular case, the final chemical composition is found to be very similar to that of the full multizone AGB model where densities up to $N_n = 2.1 \times 10^{15}$ cm^{-3} are reached.

As shown in Fig. 8, increasing the rate of ^{65}Ni(n,γ) (case 2) leads to a smaller production of ^{65}Cu (as a result of ^{65}Ni decay) by a factor of $\sim$3 in both weak and strong *i*-process cases. Lowering ^{66}Ni(n,γ) (case 3) has the strongest impact since ^{66}Ni now acts as a bottleneck. In the weak *i*-process case (Fig. 8, top panel), it leads to an overproduction of ^{66}Zn by a factor of $\sim$10 to the detriment of $70 < A < 90$ isotopes ($30 < Z < 40$), which are underproduced by a factor of $\sim$3 at maximum. For a higher neutron density (Fig. 8, bottom panel), the production of $66 < A < 135$ isotopes ($28 < Z < 54$) is enhanced by a factor of typically 2–4. The uncertainties on the nominal ^{66}Ni(n,γ) MACS obtained in this work ($\pm$5 mb at 30 keV) induce a variation of about a factor of 3 at $A = 66$ (dashed lines in Fig. 8, top panel).

Reference [17] investigated the case of a weak *i* process using one-zone models with an initial metallicity of [Fe/H] $= -1.6$ ([Fe/H] $= -2.5$ here) and different reaction rates (most of (n,γ) rates coming from the JINA REACLIB library [75]). Although the physical inputs are different, in the case of a weak *i* process the results are qualitatively similar to those of Ref. [17]: an underproduction of the elements with $32 < Z < 42$ when adopting a low ^{66}Ni(n,γ) rate.

However, when considering a full multizone AGB calculation, the impact of ^{66}Ni(n,γ) is strongly dampened (Fig. 9). The overproduction of ^{66}Zn in case 3 is clearly present but the enrichment is a factor of $\sim$3 lower. In the stellar model, multiple zones with different temperatures, densities, chemical compositions and irradiations are mixed together by convection leading to a dilute production of the elements, an effect that cannot be captured by one-zone calculations.

The impact of the ^{66}Ni(n,γ) reaction appears to be marginal in low-metallicity AGB stars experiencing *i*-process nucleosynthesis. It shows that one-zone calculations are inherently approximate and cannot guarantee to reproduce the accurate physics picture for a system. We should also emphasize that only one *i*-process site was investigated and we cannot exclude a different impact of ^{66}Ni(n,γ) in other sites such as, e.g. rapidly accreting white dwarfs [97].

VI. SUMMARY

In this paper we have presented experimental NLD and γSF of the unstable ^{67}Ni nucleus. It is the first time the Oslo method has been applied to an inverse kinematics experiment with a radioactive beam. Due to the lack of reliable nuclear data for ^{67}Ni the NLD and γSF are normalized to model predictions resulting in relatively large uncertainties. Hauser-Feshbach calculations were performed with the extracted NLD and γSF to find the neutron capture cross section of ^{66}Ni. The result of these calculations showed a rather high capture rate compared to the theoretical range, and can help improve our understanding of the *i*-process nucleosynthesis.

In agreement with Ref. [17], we find that the reaction ^{66}Ni(n,γ) acts as a bottleneck when using one-zone models. Nevertheless, the impact is strongly dampened in multizone low-metallicity AGB stellar models experiencing *i*-process nucleosynthesis. This reaction may however have a different impact in other *i*-process sites.

ACKNOWLEDGMENTS

The authors thank the accelerator team at CERN ISOLDE for providing excellent running conditions. Special thanks to Tom Berry, Lucia Crespo Campo, Themba Nogwanya, Jacob Snäll, and Khanyisa Sowazi for their contributions during the experiment. This study has been funded by the Research Council of Norway through its grants to the Norwegian Nuclear Research Centre (Project No. 341985) and the Norwegian Centre for CERN-related Research (Project No. 310713). Additional research project grants were provided by the Research Council of Norway (Grants No. 263030, No. 325714, and No. 245882), the National Research Foundation of South Africa (Grant No. 118846), the EU Horizon 2020 Framework Programme research and innovation program through ENSAR2 (Grant No. 654002), and the U.S. Department of Energy, Office of Science, Office of Nuclear Physics under Contracts No. DE-AC02-05CH11231, No. DE-AC52-07NA27344 (LBNL) and Contract No. DE-AC52-07NA27344 (LLNL). Funding was also provided by the German BMBF under Contracts No. 05P18PKCIA, No. 05P21PKCI1, and No. 05P15RDCIA, and 'Verbundprojekt' 05P18PKCI1, 05P2021. This work was supported by the Fonds de la Recherche Scientifique-FNRS under Grant No. IISN 4.4502.19. L.S. and S.G. are senior FRS-F.N.R.S. research associates and A.C. is a postdoctorate FRS-F.N.R.S. fellow. G.R. acknowledges the support by the Bulgarian Ministry of Education and Science within the National Roadmap for Research Infrastructures (object CERN). Additional support was provided by the Research Foundation Flanders (FWO, Belgium) under GOA/2015/010 (BOF KU Leuven) and the FWO and F.R.S.-FNRS under the Excellence of Science (EOS) programme (No. 40007501).

[1] P. Merrill, Technetium in the stars, Science **115**, 479 (1952).
[2] E. M. Burbidge, G. R. Burbidge, W. A. Fowler, and F. Hoyle, Synthesis of the elements in stars, Rev. Mod. Phys. **29**, 547 (1957).
[3] J. J. Cowan and W. K. Rose, Production of ^{14}C and neutrons in red giants, Astrophys. J. **212**, 149 (1977).
[4] I. U. Roederer, A. I. Karakas, M. Pignatari, and F. Herwig, The diverse origins of neutron-capture elements in the metal-poor star HD 94028: Possible detection of products of *i*-process nucleosynthesis, Astrophys. J. **821**, 37 (2016).
[5] S. Goriely, P. Dimitriou, M. Wiedeking, T. Belgya, R. Firestone, J. Kopecky, M. Krtička, V. Plujko, R. Schwengner, S. Siem, H. Utsunomiya, S. Hilaire, S. Péru, Y. S. Cho, D. M. Filipescu, N. Iwamoto, T. Kawano, V. Varlamov, and R. Xu, Reference database for photon strength functions, Eur. Phys. J. A **55**, 172 (2019).
[6] A. C. Larsen, A. Spyrou, S. N. Liddick, and M. Guttormsen, Novel techniques for constraining neutron-capture rates relevant for *r*-process heavy-element nucleosynthesis, Prog. Part. Nucl. Phys. **107**, 69 (2019).
[7] M. Wiedeking and S. Goriely, Photon strength functions and nuclear level densities: Invaluable input for nucleosynthesis, Phil. Trans. R. Soc. A. **382**, 20230125 (2024).
[8] A. Schiller, L. Bergholt, M. Guttormsen, E. Melby, J. Rekstad, and S. Siem, Extraction of level density and γ strength function from primary γ spectra, Nucl. Instrum. Methods A **447**, 498 (2000).
[9] J. E. Midtbø, F. Zeiser, E. Lima, A. C. Larsen, G. M. Tveten, M. Guttormsen, F. L. Bello Garrote, A. Kvellestad, and T. Renstrøm, A new software implementation of the Oslo method with rigorous statistical uncertainty propagation, Comput. Phys. Commun. **262**, 107795 (2021).
[10] W. Hauser and H. Feshbach, The inelastic scattering of neutrons, Phys. Rev. **87**, 366 (1952).
[11] A. Spyrou, S. N. Liddick, A. C. Larsen, M. Guttormsen, K. Cooper, A. C. Dombos, D. J. Morrissey, F. Naqvi, G. Perdikakis, S. J. Quinn, T. Renstrøm, J. A. Rodriguez, A. Simon, C. S. Sumithrarachchi, and R. G. T. Zegers, Novel technique for constraining *r*-process (n,γ) reaction rates, Phys. Rev. Lett. **113**, 232502 (2014).
[12] A. C. Larsen, J. E. Midtbø, M. Guttormsen, T. Renstrøm, S. N. Liddick, A. Spyrou, S. Karampagia, B. A. Brown, O. Achakovskiy, S. Kamerdzhiev, D. L. Bleuel, A. Couture, L. C. Campo, B. P. Crider, A. C. Dombos, R. Lewis, S. Mosby, F. Naqvi, G. Perdikakis, C. J. Prokop *et al.*, Enhanced low-energy γ-decay strength of ^{70}Ni and its robustness within the shell model, Phys. Rev. C **97**, 054329 (2018).
[13] R. Lewis, S. N. Liddick, A. C. Larsen, A. Spyrou, D. L. Bleuel, A. Couture, L. C. Campo, B. P. Crider, A. C. Dombos, M. Guttormsen, S. Mosby, F. Naqvi, G. Perdikakis, C. J. Prokop, S. J. Quinn, T. Renstrøm, and S. Siem, Experimental constraints on the ^{73}Zn$(n,\gamma)^{74}$Zn reaction rate, Phys. Rev. C **99**, 034601 (2019).
[14] S. N. Liddick, A. Spyrou, B. P. Crider, F. Naqvi, A. C. Larsen, M. Guttormsen, M. Mumpower, R. Surman, G. Perdikakis, D. L. Bleuel, A. Couture, L. Crespo Campo, A. C. Dombos, R. Lewis, S. Mosby, S. Nikas, C. J. Prokop, T. Renstrom, B. Rubio, S. Siem *et al.*, Experimental neutron capture rate constraint far from stability, Phys. Rev. Lett. **116**, 242502 (2016).
[15] S. N. Liddick, A. C. Larsen, M. Guttormsen, A. Spyrou, B. P. Crider, F. Naqvi, J. E. Midtbø, F. L. Bello Garrote, D. L. Bleuel, L. Crespo Campo, A. Couture, A. C. Dombos, F. Giacoppo, A. Görgen, K. Hadynska-Klek, T. W. Hagen, V. W. Ingeberg, B. V. Kheswa, R. Lewis, S. Mosby *et al.*, Benchmarking the extraction of statistical neutron capture cross sections on short-lived nuclei for applications using the β-Oslo method, Phys. Rev. C **100**, 024624 (2019).
[16] V. W. Ingeberg, S. Siem, M. Wiedeking, K. Sieja, D. L. Bleuel, C. P. Brits, T. D. Bucher, T. S. Dinoko, J. L. Easton, A. Görgen, M. Guttormsen, P. Jones, B. V. Kheswa, N. A. Khumalo, A. C. Larsen, E. A. Lawrie, J. J. Lawrie, S. N. Majola, K. L. Malatji, L. Makhathini *et al.*, First application of the Oslo method in inverse kinematics, Eur. Phys. J. A **56**, 68 (2020).

[17] J. E. McKay, P. A. Denissenkov, F. Herwig, G. Perdikakis, and H. Schatz, The impact of (n,γ) reaction rate uncertainties on the predicted abundances of *i*-process elements with $32 \leqslant Z \leqslant 48$ in the metal-poor star HD94028, Mon. Not. R. Astron. Soc. **491**, 5179 (2020).

[18] Y. Kadi, M. A. Fraser, and A. Papageorgiou-Koufidou, *HIE-ISOLDE: Technical Design Report for the Energy Upgrade*, edited by Y. Kadi (CERN, Geneva, 2018).

[19] V. N. Fedoseyev, G. Huber, U. Köster, J. Lettry, V. I. Mishin, H. Ravn, and V. Sebastian, The ISOLDE laser ion source for exotic nuclei, Hyperfine Interact. **127**, 409 (2000).

[20] F. Ames, G. Bollen, P. Delahaye, O. Forstner, G. Huber, O. Kester, K. Reisinger, and P. Schmidt, Cooling of radioactive ions with the Penning trap REXTRAP, Nucl. Instrum. Methods A **538**, 17 (2005).

[21] F. Wenander, EBIS as charge breeder for radioactive ion beam accelerators, Nucl. Phys. A **701**, 528 (2002).

[22] F. Wenander, Charge breeding of radioactive ions with EBIS and EBIT, J. Instrum. **5**, C10004 (2010).

[23] N. Kheswa, T. Dinoko, and M. Wiedeking, The production of deuterated polyethylene targets, EPJ Web Conf. **229**, 03003 (2020).

[24] J. Diriken, N. Patronis, A. Andreyev, S. Antalic, V. Bildstein, A. Blazhev, I. Darby, H. De Witte, J. Eberth, J. Elseviers, V. Fedosseev, F. Flavigny, C. Fransen, G. Georgiev, R. Gernhauser, H. Hess, M. Huyse, J. Jolie, T. Kröll, R. Krücken *et al.*, Study of the deformation-driving $\nu d_{5/2}$ orbital in $^{67}_{28}Ni_{39}$ using one-neutron transfer reactions, Phys. Lett. B **736**, 533 (2014).

[25] S. Hellgartner, D. Mücher, K. Wimmer, V. Bildstein, J. Egido, R. Gernhäuser, R. Krücken, A. Nowak, M. Zielińska, C. Bauer, M. Benito, S. Bottoni, H. De Witte, J. Elseviers, D. Fedorov, F. Flavigny, A. Illana, M. Klintefjord, T. Kröll, R. Lutter *et al.*, Axial and triaxial degrees of freedom in ^{72}Zn, Phys. Lett. B **841**, 137933 (2023).

[26] S. C. Hellgartner, Probing nuclear shell structure beyond the N = 40 Subshell using multiple coulomb excitation and transfer experiments, Ph.D. thesis, Technische Universität München (2015), https://mediatum.ub.tum.de/1277804.

[27] J. Eberth, G. Pascovici, H. G. Thomas, N. Warr, D. Weisshaar, D. Habs, P. Reiter, P. Thirolf, D. Schwalm, C. Gund, H. Scheit, M. Lauer, P. Van Duppen, S. Franchoo, M. Huyse, R. M. Lieder, W. Gast, J. Gerl, and K. P. Lieb, MINIBALL A Ge detector array for radioactive ion beam facilities, Prog. Part. Nucl. Phys. **46**, 389 (2001).

[28] N. Warr, J. Van de Walle, M. Albers, F. Ames, B. Bastin, C. Bauer, V. Bildstein, A. Blazhev, S. Bönig, N. Bree, B. Bruyneel, P. A. Butler, J. Cederkäll, E. Clément, T. E. Cocolios, T. Davinson, H. De Witte, P. Delahaye, D. D. DiJulio, J. Diriken *et al.*, The Miniball spectrometer, Eur. Phys. J. A **49**, 40 (2013).

[29] M. Guttormsen, T. S. Tveter, L. Bergholt, F. Ingebretsen, and J. Rekstad, The unfolding of continuum γ-ray spectra, Nucl. Instrum. Methods A **374**, 371 (1996).

[30] S. Agostinelli, J. Allison, K. Amako, J. Apostolakis, H. Araujo, P. Arce, M. Asai, D. Axen, S. Banerjee, G. Barrand, F. Behner, L. Bellagamba, J. Boudreau, L. Broglia, A. Brunengo, H. Burkhardt, S. Chauvie, J. Chuma, R. Chytracek, G. Cooperman *et al.*, GEANT4—A simulation toolkit, Nucl. Instrum. Methods A **506**, 250 (2003).

[31] V. W. Ingeberg, vetlewi/MiniballREX: Ni67, https://zenodo.org/records/6075853 (2022).

[32] M. Guttormsen, T. Ramsøy, and J. Rekstad, The first generation of γ-rays from hot nuclei, Nucl. Instrum. Methods A **255**, 518 (1987).

[33] A. C. Larsen, M. Guttormsen, M. Krtička, E. Běták, A. Bürger, A. Görgen, H. T. Nyhus, J. Rekstad, A. Schiller, S. Siem, H. K. Toft, G. M. Tveten, A. V. Voinov, and K. Wikan, Analysis of possible systematic errors in the Oslo method, Phys. Rev. C **83**, 034315 (2011).

[34] V. W. Ingeberg, P. Jones, L. Msebi, S. Siem, M. Wiedeking, A. A. Avaa, M. V. Chisapi, E. A. Lawrie, K. L. Malatji, L. Makhathini, S. P. Noncolela, and O. Shirinda, Nuclear level density and γ-ray strength function of ^{63}Ni, Phys. Rev. C **106**, 054315 (2022).

[35] A. C. Larsen, M. Guttormsen, R. Schwengner, D. L. Bleuel, S. Goriely, S. Harissopulos, F. L. Bello Garrote, Y. Byun, T. K. Eriksen, F. Giacoppo, A. Görgen, T. W. Hagen, M. Klintefjord, T. Renstrøm, S. J. Rose, E. Sahin, S. Siem, T. G. Tornyi, G. M. Tveten, A. V. Voinov *et al.*, Experimentally constrained $(p,\gamma)^{89}$Y and $(n,\gamma)^{89}$Y reaction rates relevant to *p*-process nucleosynthesis, Phys. Rev. C **93**, 045810 (2016).

[36] C. P. Brits, K. L. Malatji, M. Wiedeking, B. V. Kheswa, S. Goriely, F. L. Bello Garrote, D. L. Bleuel, F. Giacoppo, A. Görgen, M. Guttormsen, K. Hadynska-Klek, T. W. Hagen, S. Hilaire, V. W. Ingeberg, H. Jia, M. Klintefjord, A. C. Larsen, S. N. T. Majola, P. Papka, S. Péru *et al.*, Nuclear level densities and γ-ray strength functions of ^{180,181,182}Ta, Phys. Rev. C **99**, 054330 (2019).

[37] B. V. Kheswa, M. Wiedeking, F. Giacoppo, S. Goriely, M. Guttormsen, A. C. Larsen, F. L. Bello Garrote, T. K. Eriksen, A. Görgen, T. W. Hagen, P. E. Koehler, M. Klintefjord, H. T. Nyhus, P. Papka, T. Renstrøm, S. Rose, E. Sahin, S. Siem, and T. Tornyi, Galactic production of ^{138}La: Impact of ^{138,139}La statistical properties, Phys. Lett. B **744**, 268 (2015).

[38] A. Sweet, D. L. Bleuel, N. D. Scielzo, L. A. Bernstein, A. C. Dombos, B. L. Goldblum, C. M. Harris, T. A. Laplace, A. C. Larsen, R. Lewis, S. N. Liddick, S. M. Lyons, F. Naqvi, A. Palmisano-Kyle, A. L. Richard, M. K. Smith, A. Spyrou, J. Vujic, and M. Wiedeking, Nuclear level density and γ-decay strength of ^{93}Sr, Phys. Rev. C **109**, 054305 (2024).

[39] A. Spyrou, D. Mücher, P. A. Denissenkov, F. Herwig, E. C. Good, G. Balk, H. C. Berg, D. L. Bleuel, J. A. Clark, C. Dembski, P. A. DeYoung, B. Greaves, M. Guttormsen, C. Harris, A. C. Larsen, S. N. Liddick, S. Lyons, M. Markova, M. J. Mogannam, S. Nikas *et al.*, First study of the ^{139}Ba$(n,\gamma)^{140}$Ba reaction to constrain the conditions for the astrophysical *i* process, Phys. Rev. Lett. **132**, 202701 (2024).

[40] D. Mücher, A. Spyrou, M. Wiedeking, M. Guttormsen, A. C. Larsen, F. Zeiser, C. Harris, A. L. Richard, M. K. Smith, A. Görgen, S. N. Liddick, S. Siem, H. C. Berg, J. A. Clark, P. A. DeYoung, A. C. Dombos, B. Greaves, L. Hicks, R. Kelmar, S. Lyons *et al.*, Extracting model-independent nuclear level densities away from stability, Phys. Rev. C **107**, L011602 (2023).

[41] M. Wiedeking, M. Guttormsen, A. C. Larsen, F. Zeiser, A. Görgen, S. N. Liddick, D. Mücher, S. Siem, and A. Spyrou, Independent normalization for γ -ray strength functions: The shape method, Phys. Rev. C **104**, 014311 (2021).

[42] B. A. Brown and A. C. Larsen, Large low-energy M1 strength for Fe 56,57 within the nuclear shell model, Phys. Rev. Lett. **113**, 252502 (2014).

[43] M. Guttormsen, M. Aiche, F. L. Bello Garrote, L. A. Bernstein, D. L. Bleuel, Y. Byun, Q. Ducasse, T. K. Eriksen, F. Giacoppo, A. Görgen, F. Gunsing, T. W. Hagen, B. Jurado, M. Klintefjord, A. C. Larsen, L. Lebois, B. Leniau, H. T. Nyhus, T. Renstrøm, S. J. Rose *et al.*, Experimental level densities of atomic nuclei, Eur. Phys. J. A **51**, 170 (2015).

[44] L. C. Campo, A. C. Larsen, F. L. Bello Garrote, T. K. Eriksen, F. Giacoppo, A. Görgen, M. Guttormsen, M. Klintefjord, T. Renstrøm, E. Sahin, S. Siem, T. G. Tornyi, and G. M. Tveten, Investigating the γ decay of ^{65}Ni from particle-γ coincidence data, Phys. Rev. C **96**, 014312 (2017).

[45] T. Renstrøm, H. T. Nyhus, H. Utsunomiya, R. Schwengner, S. Goriely, A. C. Larsen, D. M. Filipescu, I. Gheorghe, L. A. Bernstein, D. L. Bleuel, T. Glodariu, A. Görgen, M. Guttormsen, T. W. Hagen, B. V. Kheswa, Y. W. Lui, D. Negi, I. E. Ruud, T. Shima, S. Siem *et al.*, Low-energy enhancement in the γ-ray strength functions of ^{73,74}Ge, Phys. Rev. C **93**, 064302 (2016).

[46] J. E. Midtbø, A. C. Larsen, T. Renstrøm, F. L. Bello Garrote, and E. Lima, Consolidating the concept of low-energy magnetic dipole decay radiation, Phys. Rev. C **98**, 064321 (2018).

[47] F. Feroz and M. P. Hobson, Multimodal nested sampling: An efficient and robust alternative to Markov Chain Monte Carlo methods for astronomical data analyses, Mon. Not. R. Astron. Soc. **384**, 449 (2008).

[48] F. Feroz, M. P. Hobson, and M. Bridges, MultiNest: An efficient and robust Bayesian inference tool for cosmology and particle physics, Mon. Not. R. Astron. Soc. **398**, 1601 (2009).

[49] F. Feroz, M. P. Hobson, E. Cameron, and A. N. Pettitt, Importance nested samplingand the MultiNest algorithm, The Open J. Astrophys. **2**, 10 (2019).

[50] J. Buchner, A. Georgakakis, K. Nandra, L. Hsu, C. Rangel, M. Brightman, A. Merloni, M. Salvato, J. Donley, and D. Kocevski, X-ray spectral modelling of the AGN obscuring region in the CDFS: Bayesian model selection and catalogue, Astron. Astrophys. **564**, A125 (2014).

[51] H. A. Bethe, An attempt to calculate the number of energy levels of a heavy nucleus, Phys. Rev. **50**, 332 (1936).

[52] A. Gilbert and A. G. W. Cameron, A composite nuclear-level density formula with shell corrections, Can. J. Phys. **43**, 1446 (1965).

[53] T. Ericson, A statistical analysis of excited nuclear states, Nucl. Phys. **11**, 481 (1959).

[54] S. Goriely, S. Hilaire, and A. J. Koning, Improved microscopic nuclear level densities within the Hartree-Fock-Bogoliubov plus combinatorial method, Phys. Rev. C **78**, 064307 (2008).

[55] R. Capote, M. Herman, P. Obložinský, P. G. Young, S. Goriely, T. Belgya, A. V. Ignatyuk, A. J. Koning, S. Hilaire, V. A. Plujko, M. Avrigeanu, O. Bersillon, M. B. Chadwick, T. Fukahori, Z. Ge, Y. Han, S. Kailas, J. Kopecky, V. M. Maslov, G. Reffo *et al.*, RIPL—Reference Input Parameter Library for calculation of nuclear reactions and nuclear data evaluations, Nucl. Data Sheets **110**, 3107 (2009).

[56] M. Guttormsen, S. Goriely, A. C. Larsen, A. Görgen, T. W. Hagen, T. Renstrøm, S. Siem, N. U. H. Syed, G. Tagliente, H. K. Toft, H. Utsunomiya, A. V. Voinov, and K. Wikan, Quasicontinuum γ decay of ^{91,92}Zr: Benchmarking indirect (n, γ) cross-section measurements for the s process, Phys. Rev. C **96**, 024313 (2017).

[57] S. Goriely and V. Plujko, Simple empirical $E1$ and $M1$ strength functions for practical applications, Phys. Rev. C **99**, 014303 (2019).

[58] S. Goriely, S. Hilaire, S. Péru, and K. Sieja, Gogny-HFB+QRPA dipole strength function and its application to radiative nucleon capture cross section, Phys. Rev. C **98**, 014327 (2018).

[59] S. Hilaire and M. Girod, Large-scale mean-field calculations from proton to neutron drip lines using the D1S Gogny force, Eur. Phys. J. A **33**, 237 (2007).

[60] R. Schwengner, S. Frauendorf, and A. C. Larsen, Low-energy enhancement of magnetic dipole radiation, Phys. Rev. Lett. **111**, 232504 (2013).

[61] S. Frauendorf and R. Schwengner, Evolution of low-lying $M1$ modes in germanium isotopes, Phys. Rev. C **105**, 034335 (2022).

[62] K. Sieja, Electric and magnetic dipole strength at low energy, Phys. Rev. Lett. **119**, 052502 (2017).

[63] M. D. Jones, A. O. Macchiavelli, M. Wiedeking, L. A. Bernstein, H. L. Crawford, C. M. Campbell, R. M. Clark, M. Cromaz, P. Fallon, I. Y. Lee, M. Salathe, A. Wiens, A. D. Ayangeakaa, D. L. Bleuel, S. Bottoni, M. P. Carpenter, H. M. Davids, J. Elson, A. Görgen, M. Guttormsen *et al.*, Examination of the low-energy enhancement of the γ-ray strength function of ^{56}Fe, Phys. Rev. C **97**, 024327 (2018).

[64] D. M. Rossi, P. Adrich, F. Aksouh, H. Alvarez-Pol, T. Aumann, J. Benlliure, M. Böhmer, K. Boretzky, E. Casarejos, M. Chartier, A. Chatillon, D. Cortina-Gil, U. Datta Pramanik, H. Emling, O. Ershova, B. Fernandez-Dominguez, H. Geissel, M. Gorska, M. Heil, H. T. Johansson *et al.*, Measurement of the dipole polarizability of the unstable neutron-rich nucleus ^{68}Ni, Phys. Rev. Lett. **111**, 242503 (2013).

[65] See Supplemental Material at http://link.aps.org/supplemental/10.1103/PhysRevC.111.015803 for numerical values of prior and posterior PDFs.

[66] T. Von Egidy, H. H. Schmidt, and A. N. Behkami, Nuclear level densities and level spacing distributions: Part II, Nucl. Phys. A **481**, 189 (1988).

[67] T. von Egidy and D. Bucurescu, Systematics of nuclear level density parameters, Phys. Rev. C **72**, 044311 (2005).

[68] T. von Egidy and D. Bucurescu, Experimental energy-dependent nuclear spin distributions, Phys. Rev. C **80**, 054310 (2009).

[69] H. Junde, H. Xiaolong, and J. K. Tuli, Nuclear data sheets for A = 67, Nucl. Data Sheets **106**, 159 (2005).

[70] J. Diriken, N. Patronis, A. Andreyev, S. Antalic, V. Bildstein, A. Blazhev, I. G. Darby, H. De Witte, J. Eberth, J. Elseviers, V. N. Fedosseev, F. Flavigny, C. Fransen, G. Georgiev, R. Gernhauser, H. Hess, M. Huyse, J. Jolie, T. Kröll, R. Krücken *et al.*, Experimental study of the ^{66}Ni(d,p)^{67}Ni one-neutron transfer reaction, Phys. Rev. C **91**, 054321 (2015).

[71] A. J. Koning, S. Hilaire, and M. C. Duijvestijn, TALYS-1.0, in *ND2007* (EDP Sciences, Les Ulis, France, 2007), pp. 211–214.

[72] A. J. M. Plompen, O. Cabellos, C. De Saint Jean, M. Fleming, A. Algora, M. Angelone, P. Archier, E. Bauge, O. Bersillon, A. Blokhin, F. Cantargi, A. Chebboubi, C. Diez, H. Duarte, E. Dupont, J. Dyrda, B. Erasmus, L. Fiorito, U. Fischer, D.

Flammini *et al.*, The joint evaluated fission and fusion nuclear data library, JEFF-3.3, Eur. Phys. J. A **56**, 181 (2020).

[73] A. Koning, D. Rochman, J.-C. Sublet, N. Dzysiuk, M. Fleming, and S. van der Marck, TENDL: Complete nuclear data library for innovative nuclear science and technology, Nucl. Data Sheets **155**, 1 (2019).

[74] D. Rochman, A. Koning, and J.-C. Sublet, A statistical analysis of evaluated neutron resonances with TARES for JEFF-3.3, JENDL-4.0, ENDF/B-VIII.0 and TENDL-2019, Nucl. Data Sheets **163**, 163 (2020).

[75] R. H. Cyburt, A. M. Amthor, R. Ferguson, Z. Meisel, K. Smith, S. Warren, A. Heger, R. D. Hoffman, T. Rauscher, A. Sakharuk, H. Schatz, F. K. Thielemann, and M. Wiescher, The jina reaclib database: Its recent updates and impact on type-i x-ray bursts, Astrophys. J. Suppl. Series **189**, 240 (2010).

[76] M. Arnould and S. Goriely, Microscopic nuclear models for astrophysics: The Brussels bruslib nuclear library and beyond, Nucl. Phys. A **777**, 157 (2006).

[77] A. Koning and J. Delaroche, Local and global nucleon optical models from 1 keV to 200 MeV, Nucl. Phys. A **713**, 231 (2003).

[78] E. Bauge, J. P. Delaroche, and M. Girod, Lane-consistent, semimicroscopic nucleon-nucleus optical model, Phys. Rev. C **63**, 024607 (2001).

[79] P. Denissenkov, G. Perdikakis, F. Herwig, H. Schatz, C. Ritter, M. Pignatari, S. Jones, S. Nikas, and A. Spyrou, The impact of (n,γ) reaction rate uncertainties of unstable isotopes near $N = 50$ on the *i*-process nucleosynthesis in He-shell flash white dwarfs, J. Phys. G: Nucl. Part. Phys. **45**, 055203 (2018).

[80] H. Utsunomiya, T. Renstrøm, G. M. Tveten, S. Goriely, S. Katayama, T. Ari-izumi, D. Takenaka, D. Symochko, B. V. Kheswa, V. W. Ingeberg, T. Glodariu, Y.-W. Lui, S. Miyamoto, A. C. Larsen, J. E. Midtbø, A. Görgen, S. Siem, L. C. Campo, M. Guttormsen, S. Hilaire *et al.*, Photoneutron cross sections for Ni isotopes: Toward understanding (n,γ) cross sections relevant to weak s-process nucleosynthesis, Phys. Rev. C **98**, 054619 (2018).

[81] L. Crespo Campo, F. L. Bello Garrote, T. K. Eriksen, A. Görgen, M. Guttormsen, K. Hadynska-Klek, M. Klintefjord, A. C. Larsen, T. Renstrøm, E. Sahin, S. Siem, A. Springer, T. G. Tornyi, and G. M. Tveten, Statistical γ-decay properties of ^{64}Ni and deduced (n,γ) cross section of the s-process branch-point nucleus ^{63}Ni, Phys. Rev. C **94**, 044321 (2016).

[82] A. Spyrou, A. C. Larsen, S. N. Liddick, F. Naqvi, B. P. Crider, A. C. Dombos, M. Guttormsen, D. L. Bleuel, A. Couture, L. C. Campo, R. Lewis, S. Mosby, M. R. Mumpower, G. Perdikakis, C. J. Prokop, S. J. Quinn, T. Renstrom, S. Siem, and R. Surman, Neutron-capture rates for explosive nucleosynthesis: The case of ^{68}Ni(n,γ)^{69}Ni, J. Phys. G: Nucl. Part. Phys. **44**, 044002 (2017).

[83] R. Schwengner, S. Frauendorf, and B. A. Brown, Low-energy magnetic dipole radiation in open-shell nuclei, Phys. Rev. Lett. **118**, 092502 (2017).

[84] M. Guttormsen, K. O. Ay, M. Ozgur, E. Algin, A. C. Larsen, F. L. Bello Garrote, H. C. Berg, L. Crespo Campo, T. Dahl-Jacobsen, F. W. Furmyr, D. Gjestvang, A. Görgen, T. W. Hagen, V. W. Ingeberg, B. V. Kheswa, I. K. B. Kullmann, M. Klintefjord, M. Markova, J. E. Midtbø, V. Modamio *et al.*, Evolution of the γ-ray strength function in neodymium isotopes, Phys. Rev. C **106**, 034314 (2022).

[85] N. Iwamoto, T. Kajino, G. J. Mathews, M. Y. Fujimoto, and W. Aoki, Flash-driven convective mixing in low-mass, metal-deficient asymptotic giant branch stars: A new paradigm for lithium enrichment and a possible s-process, Astrophys. J. **602**, 377 (2004).

[86] S. Cristallo, L. Piersanti, O. Straniero, R. Gallino, I. Domínguez, and F. Käppeler, Asymptotic-giant-branch models at very low metallicity, Publ. Astron. Soc. Aust. **26**, 139 (2009).

[87] T. Suda and M. Y. Fujimoto, Evolution of low- and intermediate-mass stars with [Fe/H] $\leqslant -2.5$, Mon. Not. R. Astron. Soc. **405**, 177 (2010).

[88] R. J. Stancliffe, D. S. P. Dearborn, J. C. Lattanzio, S. A. Heap, and S. W. Campbell, Three-dimensional hydrodynamical simulations of a proton ingestion episode in a low-metallicity asymptotic giant branch star, Astrophys. J. **742**, 121 (2011).

[89] A. Choplin, L. Siess, and S. Goriely, The intermediate neutron capture process. I. Development of the *i*-process in low-metallicity low-mass AGB stars, Astron. Astrophys. **648**, A119 (2021).

[90] L. Siess, E. Dufour, and M. Forestini, An internet server for pre-main sequence tracks of low- and intermediate-mass stars, Astron. Astrophys. **358**, 593 (2000).

[91] L. Siess, Evolution of massive AGB stars. I. Carbon burning phase, Astron. Astrophys. **448**, 717 (2006).

[92] S. Goriely and L. Siess, Sensitivity of the s-process nucleosynthesis in AGB stars to the overshoot model, Astron. Astrophys. **609**, A29 (2018).

[93] http://www.astro.ulb.ac.be/bruslib/.

[94] Y. Xu, S. Goriely, A. Jorissen, G. Chen, and M. Arnould, Databases and tools for nuclear astrophysics applications: Brussels nuclear library (BRUSLIB), nuclear astrophysics compilation of reactions II (NACRE II) and nuclear network generator (NETGEN), Astron. Astrophys. **549**, A106 (2013).

[95] S. Goriely, L. Siess, and A. Choplin, The intermediate neutron capture process. II. Nuclear uncertainties, Astron. Astrophys. **654**, A129 (2021).

[96] A. Choplin, L. Siess, and S. Goriely, The intermediate neutron capture process. III. The *i*-process in AGB stars of different masses and metallicities without overshoot, Astron. Astrophys. **667**, A155 (2022).

[97] P. A. Denissenkov, F. Herwig, U. Battino, C. Ritter, M. Pignatari, S. Jones, and B. Paxton, I-process nucleosynthesis and mass retention efficiency in He-shell flash evolution of rapidly accreting white dwarfs, Astrophys. J. Lett. **834**, L10 (2017).